

# Camera for QUasars in EARly uNiverse (CQUEAN)

Won-Kee Park<sup>1,2</sup>

<sup>1</sup> CEOU/Department of Physics and Astronomy, Seoul National University, Seoul 151-742, Korea

<sup>2</sup> Korea Astronomy and Space Science Institute, Daejeon 305-348, Korea

wkpark@astro.snu.ac.kr

Soojong Pak<sup>3,4</sup>

<sup>3</sup> School of Space Research, Kyung Hee University, Gyeonggi-Do 446-741, Korea

<sup>4</sup> Department of Astronomy, University of Texas at Austin, Austin, TX 78717

soojong@khu.ac.kr

Myungshin Im<sup>1</sup>, Changsu Choi<sup>1</sup>, Yiseul Jeon<sup>1</sup>

<sup>1</sup> CEOU/Department of Physics and Astronomy, Seoul National University, Seoul 151-742, Korea

mim@astro.snu.ac.kr, changsu@astro.snu.ac.kr, ysjeon@astro.snu.ac.kr

Seunghyuk Chang

chang@offaxis.co.kr

Hyeonju Jeong<sup>3</sup>, Juhee Lim<sup>3</sup>,  
and

Eunbin Kim<sup>3</sup>

<sup>3</sup> School of Space Research, Kyung Hee University, Gyeonggi-Do 446-741, Korea

jhyeonju@khu.ac.kr, juheelim@khu.ac.kr, ebkim@khu.ac.kr

## ABSTRACT

We describe the overall characteristics and the performance of an optical CCD camera system, Camera for QUasars in EARly uNiverse (CQUEAN), which is being used at the 2.1 m Otto Struve Telescope of the McDonald Observatory since 2010 August. CQUEAN was developed for follow-up imaging observations of red sources such as high redshift quasar candidates ( $z \gtrsim 5$ ), Gamma Ray Bursts, brown dwarfs, and young stellar objects. For efficient observations of the red objects, CQUEAN has a science camera with a deep depletion CCD chip which boasts a higher quantum efficiency at  $0.7 - 1.1 \mu\text{m}$  than conventional CCD chips. The camera was developed in a short time scale ( $\sim$ one year), and has been working reliably. By employing an auto-guiding system and a focal reducer to enhance the field of view on the classical Cassegrain focus, we achieve a stable guiding in 20 minute exposures, an imaging quality with  $\text{FWHM} \geq 0.6''$  over the whole field ( $4.8' \times 4.8'$ ), and a limiting magnitude of  $z = 23.4$  AB mag at  $5\text{-}\sigma$  with one hour total integration time.

*Subject headings:* Instrumentation: photometers – Stars: variables: general – Galaxies: photometry – quasars: general

## 1. INTRODUCTION

Recent emphasis on the distant and/or obscured target observation requires near infrared (NIR) sensitive imaging devices. Although the conventional CCD chips, especially the back illuminated, thinned CCD chips, are very sensitive over a wide wavelength range ( $0.4 - 0.8 \mu\text{m}$ ), most of them are not sensitive in NIR bands, with the quantum efficiency (QE) of order of a few percent at  $\sim 1 \mu\text{m}$  (e.g., Im et al. 2010a). Detectors made of low band-gap semiconductor materials such as HgCdTe and InSb offer high sensitivity in NIR, but the NIR arrays are expensive in cost, and have strict export restrictions, making them less accessible to many astronomical imaging applications. Considering the recent high demand for NIR imaging, it is thus important to develop a cost-effective imaging camera.

To facilitate imaging out to  $1.1 \mu\text{m}$  at a reasonable cost and within a fast development schedule, the Center for the Exploration of the Origin of the Universe (CEOU) has developed a CCD camera system, Camera for QUasars in EARly uNiverse (CQUEAN). It is a camera system designed primarily for the observation of high redshift quasar candidates. The design goal was to make a camera sensitive at  $0.7 - 1.1 \mu\text{m}$  ( $\text{QE} > 20\%$  at  $1 \mu\text{m}$ ) with a moderate field of view (at least a few arcmin across). The sensitivity in the red is governed by the need for the detection of the Lyman break of objects at  $z \gtrsim 5$ . The requirement for the field of view is to allow photometry based on the reference stars available from large area surveys such as the Sloan Digital Sky Survey (SDSS) (York et al. 2000) and the Large Area Survey of UKIRT Infrared Deep Sky Survey (UKIDSS) (Lawrence et al. 2007). The optical performance requirement was to obtain the seeing limited point spread function (PSF) with FWHM better than  $1''$ .

Based on these requirements, we adopted a CCD camera with a deep depletion chip, a focal reducer, and an auto-guiding system. The development of CQUEAN started in the summer of 2009, and it was installed on the Cassegrain focus of the 2.1 m Otto Struve telescope at the McDonald Observatory, Texas, USA, on 2010 August 12. Since its commissioning run, CQUEAN has been used for various scientific projects.

In this paper, we describe the overall characteristics of CQUEAN, and its performance based on the first year of the scientific operation. Section 2 describes the overview of the instruments including the science camera, its filters, and the parameters of CQUEAN on the 2.1 m telescope. In Section 3, we describe various characteristics of the camera and images obtained with CQUEAN. We report the performance of CQUEAN in Section 4, and briefly describe the scientific result obtained with CQUEAN in Section 5. Finally, summary and conclusion are presented in Section 6.

## 2. INSTRUMENT DESCRIPTION

The main units of CQUEAN are: a science camera, a filter wheel that houses seven filters, a focal reducer, and an auto-guide camera. The auto-guide camera is mounted on a rotating arm to secure a large off-axis field of view (Kim et al. 2011). Fig. 1 shows the overall structure of CQUEAN system. An enclosure holding the science camera system, the guide camera system as well as a motor to move the guide camera were made with several pieces of aluminum. The whole system is operated by a custom-made software package on a linux-running computer which is mounted next to the main units. The observers access the control computer over network during observations. We describe each unit in detail below.

### 2.1. Science camera

CQUEAN uses an iKon-M M934 BR-DD model from Andor Technology PLC<sup>1</sup>, as its main science camera. It uses an E2V  $1024 \times 1024$  pixel deep-depletion CCD as its detector. This CCD shows a higher red sensitivity than conventional back-illuminated thinned CCDs, and also shows little fringe pattern as described later. In addition to the CCD chip, the camera contains a readout electronics, and the cooling unit inside the camera body. A fused silica window and a mechanical shutter are installed in front of the CCD chip. The camera is connected to the control computer via USB port, which makes it easy for us to handle but limits the cable length between the camera body and the computer.

---

<sup>1</sup><http://www.andor.com>

A thermoelectric cooler is used in the camera, which can cool down the chip to  $-80^{\circ}\text{C}$ . However, after reviewing performance test from the chip manufacturer, we decided to operate the camera at  $-70^{\circ}\text{C}$  because the higher operating temperature improves QE at longer wavelengths. Even at this higher operating temperature, the dark current is still comparable to the sky background.

The pixel readout speed and preamp gain can be set to three different values, respectively. After several tests, we decided to operate the camera with the pixel readout speed of 1 MHz, and with the preamp gain of 1. Under these settings, it takes about one second to read the whole pixels. A summary of the technical specification of the camera is listed in Table 1.

A generic curve of the QE of the chip at  $-100^{\circ}\text{C}$  is shown in Fig. 2 with a thick dashed line, which is taken from the manufacturer’s brochure. The characteristics of deep depletion E2V chips suggests that the QE increase by 25 % at  $1\ \mu\text{m}$  when the chip temperature is warmer by  $30^{\circ}\text{C}$  at the expense of a reduced sensitivity at the blue end according to the manufacturer. Since the operating temperature for CQUEAN was set to  $-70^{\circ}\text{C}$ , the actual QE at long wavelength is higher by a factor of 1.2 than shown in the figure.

## 2.2. Filters

In front of the science camera, we installed a commercial filter wheel, CFW-1-8, made by the Finger Lake Instrumentation (FLI)<sup>2</sup>, USA. This wheel houses eight circular filters with a diameter of 28 mm and a thickness of 5 mm.

We installed seven filters, and one black anodized aluminum plate for a calibration purpose. The seven filters are  $g$ ,  $r$ ,  $i$ ,  $z$ ,  $Y$ ,  $is$ , and  $iz$ , which were manufactured by Asahi Spectra Co., Ltd.<sup>3</sup> The  $g$ ,  $r$ , and  $i$  filters are very similar to those for SDSS (Fukugita et al. 1996), while our  $z$  filter has a transmission curve identical to that of the LSST Z-filter, which cuts off photons beyond  $0.92\ \mu\text{m}$ . The  $Y$ -band filter is identical to LSST Y-band filter whose bandwidth is narrower than that described in Hillenbrand et al. (2002) in order to minimize the contamination by telluric OH emission lines. The custom designed  $is$  and

$iz$  filters have bandwidths of  $\sim 100\ \text{\AA}$ , and their passbands are located between  $r$  and  $i$ , and  $i$  and  $z$ , respectively. They are designed to detect the quasar candidates at redshift of  $5.0 < z < 5.7$ , since SDSS  $r$ ,  $i$  and  $z$  filter colors have difficulty in distinguishing these quasars from the Galactic cool stars.

Fig. 2 shows the transmission curves of our filters as well as the QE of the CCD. It can be seen that CQUEAN does have an excellent throughput even at  $Y$ -band range, compared to other typical optical CCDs.

## 2.3. Focal reducer

The 2.1 m telescope has a focal ratio of  $f/13.65$  at its classical Cassegrain focus. This large focal ratio would result in the field of view of  $1.6' \times 1.6'$  for our science camera without a re-imaging optics, which is not adequate for our scientific purposes. The pixel scale of  $0.094''/\text{pix}$  is also too small for the seeing condition at the McDonald Observatory which is  $0.7'' - 1.2''$  in  $V$ -band.

We made a custom focal reducer to enlarge the field of view as well as to correct optical aberrations, especially for coma. Considering the seeing size, it is designed to reduce the effective focal length by three fold. In this configuration, the corresponding pixel scale is  $0.28''/\text{pix}$ , so that 3 – 4 pixels can cover the FWHM of a stellar profile under a typical seeing condition. The field of view of the system becomes  $4.8' \times 4.8'$ .

In order to reduce the optical complexity, we did not seriously consider the chromatic aberration. The focal reducer consists of four lenses and is optimized for the wavelengths between  $0.8$  and  $1.1\ \mu\text{m}$ . Fig. 3 shows the side view of the reducer optics. The first three elements reduce the focal length while correcting coma aberration of the telescope. The last element corrects the residual astigmatism and field curvature. A summary of the reducer optics is given in Table 2. Also, the spot diagrams for each wavelength band are shown in Fig. 4. All air to glass surfaces are coated to reduce the reflections for incident light of  $0.8 - 1.1\ \mu\text{m}$  wavelength band (Lim et al. 2012). Reflections for the light outside this wavelength band were not considered since the optical performance of the reducer was optimized for  $0.8 - 1.1\ \mu\text{m}$  band only. Therefore, the anti-

<sup>2</sup><http://www.flcamera.com>

<sup>3</sup><http://www.asahi-spectra.co.jp>

reflection (AR) coating substantially reduces the throughput for wavelength bands shorter than  $i$ -band. The optical components in the focal reducer was manufactured by Green Optics Co., Ltd.<sup>4</sup>

Analysis of the test images obtained during the engineering run reveals that the focal reducer indeed works as expected: the images in  $i$ ,  $z$ , and  $Y$ -bands are perfect within the seeing limits, while those in  $g$  and  $r$ -bands show coma aberrations on the peripheries of the fields. Because we did not consider the fields at four diagonal corners of the field of view, some vignetting pattern arises at all corners. This vignetting can be reduced by flat-fielding to a certain degree, but four corners of the chip are not recommended for scientific use. Section 4.1 describes the characteristics of the image profile of the CQUEAN optical system. Detailed description on the fabrication of the focal reducer and its performance is given by Lim et al. (2012).

#### 2.4. Guide camera

As described in Kim et al. (2011), the 2.1 m telescope shows tracking errors which can be removed by feedback correction in every few seconds. We made an auto-guiding system for CQUEAN and the telescope by installing an off-axis guide camera. ProLine 1001E model from the Finger Lakes Instrumentation was used as a guide CCD camera. It has a  $1024 \times 1024$  pixel CCD chip with pixel size of  $24 \mu m \times 24 \mu m$ . It is cooled to  $-30^\circ C$  with thermoelectric cooling unit during the operation. An off-axis pick-up mirror is installed to feed an off-axis field of the 2.1 m telescope to the guide camera. There is no additional optics for the guide camera, except a baffle to block the stray light into the optical path between the mirror and the guide camera. Direct imaging of an off-axis field results in the pixel scale of  $0.174''/\text{pixel}$ , and the total field of view of  $2.97' \times 2.97'$ . The expected number of guide stars brighter than limiting magnitude for one second exposure on the field of view is about one in the fields of galactic pole region, which may make auto-guiding impossible due to a lack of adequate guide stars. Therefore we use a rotating arm for the whole guide camera system to increase the size of the viewable off-axis field by a factor of five. The arm assembly is moved with

a stepping motor located behind the science camera (see Fig. 5). Both the guide camera and the moving mechanism are controlled with the same computer.

#### 2.5. Operating software

The observers need to control several components of CQUEAN to obtain the imaging data. They also need a quick and efficient way to check the quality of the acquired data on the spot. Therefore, we developed a GUI program for CQUEAN users which is easy to use, while providing functionalities sufficient to acquire the scientific data.

The program is written in Python version 2.6.5 for easy development and maintenance. The front-end GUI is developed in-house with `wxPython` library, while the low-level instrument control libraries are supplied by vendors of the science camera and the filter wheel. To access C-based SDK libraries with python, `ctypes` package was used. In addition to those, `NumPy` (math library) and `matplotlib` (graphic library) are required for the mathematical analysis routines used in the software, and `PySerial` for serial communication with the motor for the guide camera arm.

The control program runs on a linux computer running CentOS 5.5, and it requires X Window System for displaying the GUI components of the program. Its GUI consists of two windows: the CQUEAN Control window and the Quick-Look window. With the CQUEAN Control window, one can control all the CQUEAN components to acquire the imaging data: the science camera, the filter wheel, and the guide camera moving mechanism. It displays the current status of these components. In addition, it interacts with Telescope Control System (TCS) of the telescope to obtain the current pointing information of the telescope. The Quick-Look window displays the acquired image data on the screen. It has quick analysis features of displaying the contour/radial profile of a source selected with a click on the displayed image. Fig. 6 shows the two windows of CQUEAN control program. The imaging data are saved with 32 bit integer values to a FITS format file (Wells et al. 1981) after adding various header keywords to facilitate data reduction.

The auto-guiding software, *agdr*, runs on the

<sup>4</sup><http://www.greenopt.com>

same linux PC that runs the CQUEAN control program. It has been used for the auto-guiding of the 2.7 m telescope at the McDonald Observatory. A modified version for CQUEAN was supplied by P. Sam Odoms of the McDonald Observatory. The *agdr* controls the guide camera to obtain images of a guide star with 1 – 5 second exposures, depending on the brightness of the guide stars. It determines the position of the guide star on a frame, and calculates offsets of the position with respect to the position of the guide star on a reference frame. Then the *agdr* interacts with TCS of the 2.1 m telescope to correct the drift based on the offset obtained. The program repeats the procedures until the data acquisition with the science camera is completed. The auto-guiding performance was tested up to 1200 seconds of exposure. The test shows that auto-guiding with 1200 second exposure does not introduce any serious tracking errors (Kim et al. 2011). We expect that longer exposures are possible without much trouble, although we expect that most users use exposures not much longer than 1200 seconds.

The *agdr* software is also useful for monitoring the seeing condition and the atmospheric transparency of the night, since it keeps updating the FWHM and instrumental magnitude of the guide star on a plot.

### 3. CHARACTERISTICS OF CQUEAN

CQUEAN saw its first light during the engineering run carried out at the McDonald Observatory from 2010 August 10 to 17. Fig. 5 shows CQUEAN attached to the 2.1 m telescope. During the engineering run, we calibrated our guide camera system so that it can auto-guide the telescope correctly. Bias and dark images of the science camera were taken under several different temperatures to check the temperature dependencies, though most of subsequent calibration and scientific observations were carried out with the temperature set to  $-70$  °C. Various readout modes were tried to determine the best mode for scientific observation in consideration of both the time overhead and the readout noise level. Several twilight flats and dome flats were obtained, and we also investigated science camera linearity range and calibration procedure.

#### 3.1. Bias

Bias images were taken to examine the stability in the DC offset during the observing nights. They were obtained during the beginning and the end of each night, and also just before and after observations of each science target.

The examination of bias images revealed that no particular patterns are seen in a single bias image, and pixel values are uniform all over the region with a standard deviation of  $\sim 8.2$  ADU which is basically the readout noise. However, the bias level shows a small amount of inter- and intra-night variability, which may originate from the temperature variation of the chip or from the electrical instability. Fig. 7 shows the mean pixel value of single bias images during three nights in 2011 August run against the chip temperature. The bias level fluctuated during the run from about 4444 up to 4472 ADUs. Although there are scatters among the samples, and differences among each night, the bias level turned out to increase as the chip temperature gets lower. The chip temperature is controlled by turning on and off the thermoelectric cooler, and the frequency of the operation depends on the ambient temperature. Therefore, we suspect that the temperature-sensitive variations in the bias level is originating from the temperature-sensitive electronic components of the camera. Fig. 7 shows that the one degree change in temperature resulted in  $\sim 6$  ADU in the mean bias level, although the change is not entirely predictable. Short-term variation over one hour timespan is less than  $\sim 6$  ADU, so the interim solution for the bias level fluctuation would be to use bias images taken right before and after the observation of a target. In future, we hope to introduce an overscan area to correct for the bias level variation. For now, we suggest to take bias images before and after the observation of a target. Since it takes only one second to read a bias image, this does not introduce much overhead.

#### 3.2. Dark

To correct for the dark current signal, the dark images are usually taken before the start or at the end of observation every night, with exposure times equivalent to those of science images. Fig. 8 shows an example of bias subtracted dark images taken with CQUEAN with 300 second exposure.

The dark level is slightly higher in central columns than at the edges. But except for this feature, dark image shows a relatively uniform pixel value distribution over the image. The mean dark level was measured to be  $0.23 \pm 0.01$  electrons/sec/pixel, with the CCD chip at  $-70^\circ\text{C}$ .

During a night in the 2010 August run, we obtained dark images under various temperatures:  $-40^\circ\text{C}$ ,  $-50^\circ\text{C}$ ,  $-60^\circ\text{C}$ , and  $-70^\circ\text{C}$ . Fig. 9 shows the result of our experiment. The dark level increases exponentially as a function of the operating temperature. The operating temperature is optimized so that the camera provides a good throughput at  $1\ \mu\text{m}$  while keeping the dark current at a level significantly lower than the sky background. The sky count was found to be the lowest at  $\sim 1$  ADU/sec/pixel in  $g$ -band, and 3.8 ADU/sec/pixel in  $Y$ -band.

Fig. 10 shows the improvement in the signal to noise ratio (S/N) for a sky-limited observation of a faint point source ( $> 20$  AB mag) with long exposures ( $\sim 300$  seconds). Here we assume an aperture magnitude of a point source with the seeing of  $\text{FWHM} = 1''$  and a circular aperture size of  $1.7''$  diameter. The background level is assumed for the bright night ( $6.2$  DN/sec/pixel for  $Y$ -band). Once the object flux is much less than the sky noise, the result does not depend on the exact value of the object flux. The QE of the camera at  $1\ \mu\text{m}$  is set to increase linearly with respect to its temperature as follows. The equation is derived by utilizing the data from the manufacturer about the increase in the relative QE values as a function of temperature for a typical deep depletion device:

$$QE(T)/QE(-100) = 2.003 + 0.0099T$$

where  $QE(-100)$  denotes the QE at  $-100^\circ\text{C}$  which is measured to be 0.2 from the camera manufacturer's brochure. The dark current level is assumed to be as shown in Fig. 9, and sky count of 6.8 DN/sec/pixel in  $Y$ -band, respectively. Observation efficiency improves by nearly 12 % and reaches its peak at around  $-67^\circ\text{C}$  due to the increase in QE as a function of the temperature but degrades rapidly due to larger dark current level at higher temperatures. Hence, we set the operating temperature of the camera to  $-70^\circ\text{C}$ .

### 3.3. Flat field

On each clear night, we obtained twilight flat images at the start and the end of the observation. The exposure times were longer than five seconds to avoid any shutter pattern (See Section 3.5). These flat images are analyzed to understand how stable the flat fields are.

Examples of flat images in  $g$ ,  $r$ , and  $Y$ -bands are shown in Fig. 11. Vignetting can be seen in all these flat images at four corners of the chip, which is caused by a limited size of the focal reducer and the filters as described in Section 2.3. We note that the vignetting pattern changes from run to run, depending on how the focal reducer was aligned to the camera at the start of each run. Therefore, we recommend the users to use flat field images taken in the same run. Note that the  $g$  and  $r$ -band flat images show diagonal line patterns across the whole area. And the  $r$ -band flat images show stronger tendency of limb brightening than in all the other bands. These patterns in  $g$  and  $r$ -band images may arise from the degraded AR coatings of the focal reducer lenses which are optimized for wavelength band of  $0.8 - 1.1\ \mu\text{m}$ . Flat images in all the other bands look similar to the  $Y$ -band flat image shown in the right panel of the Fig. 11, such that they show faint cross pattern across the image. Although the origin of each pattern is not known, most of these patterns are removed in the final flattened images.

Fig. 12 shows the distributions of normalized pixel values of flat field images inside a square box that excludes four vignetted regions. Ten twilight flat frames with pixel values higher than 10,000 ADU were used for the flat field construction in each band, and the expected level of sky noise is about 1 - 2 %. The figure shows that the pixel sensitivity variation is of order of a few percent for the filters other than  $g$  and  $r$ , meaning that typical pixel-to-pixel sensitivity variation is very small. As for the  $g$ -band flat image, the pixel value distribution shows a peak higher than the normalized value due to the bright diagonal line patterns across its image. Similarly, the  $r$ -band flat shows a broader pixel value distribution since it shows a strong tendency of limb brightening than other band flats.

We compared the flat field images on four different nights during a single observing run to see

how much the flat field patterns vary from night to night. Fig. 13 shows examples of a flat image from one night divided by another flat image taken on a different night. If there were no variation among flats, the divided images would be very flat. However, it can be seen that vignetting pattern is clearly visible at the edge of the image, and a gradient is seen across the image, of the peak to peak variation is as large as  $\sim 1.5\%$  in some cases. Similar patterns are seen among the evening flat images divided by the morning flats taken on the same nights on some nights. The variation of patterns is caused by the very small alignment change of focal reducer and the position change of the filters. Observers have to pay special attention in setting up the instrument properly at the beginning of each run/night. Based on these results, observers are recommended to use the twilight flat images taken at the same night.

Fig. 14 shows the stacked images of six 300 second *i*-band exposures each flattened with a twilight flat image and a dome flat image taken on the same night. The twilight flat images were obtained with 5 second exposure, and the dome flat images with 5.5 seconds, to avoid the shutter pattern while securing enough high signals. Due to the curvature of the dome, the illumination of the dome flat light turns out to be slightly brighter in the lower part than the other half. We ran SExtractor (Bertin & Arnouts 1996) on two images to see the difference in the photometry, which is shown in panel (a) of Fig. 15. We did not find any significant difference between two results for stars which S/N is greater than 10. No change in magnitude difference is seen along the vertical axis, either. There are large scatters in upper and lower end of the chip ( $Y \leq 250$  or  $Y \geq 750$ ), but all of them are found to be in the vignetted region. The difference in sky background between two images turned out to get larger in the outskirts than in the central region, which was found to be  $0.7 - 1.5\%$  at the edge. Since edge region is not recommended for photometry due to vignetting, the sky difference would not be an important issue in practice.

### 3.4. Gain and readout noise

The system electronics gain and its readout noise can be measured from its image. From a pair of flat images and bias images, both quantities can be measured with the following formulae

(Birney et al. 2006):

$$\text{gain} = \frac{(\bar{F}_1 + \bar{F}_2) - (\bar{B}_1 + \bar{B}_2)}{(\sigma_{F_1-F_2}^2) - (\sigma_{B_1-B_2}^2)}$$

$$\text{Readout noise} = \frac{1}{\sqrt{2}} \cdot \text{gain} \cdot (\sigma_{B_1-B_2})$$

where  $\bar{F}_1$  and  $\bar{F}_2$  are mean pixel values of the two flat images, and  $\bar{B}_1$ ,  $\bar{B}_2$  the mean pixel values for two bias images.  $\sigma_{F_1-F_2}^2$  and  $\sigma_{B_1-B_2}^2$  denote the variance of the pixel values of the difference images,  $F_1 - F_2$  and  $B_1 - B_2$ , respectively.

Using a pair of *r*-band flats and bias images obtained during the 2010 August run, we calculated the readout noise and the gain value of the camera. The gain and the readout noise are  $1.0 \pm 0.1$  electrons/ADU, and  $8.2 \pm 0.1$  electrons/pixel, respectively.

We also checked whether the readout noise depends on the chip temperature, by examining the standard deviation of mean pixel values of bias images taken under four different temperatures in 2010 August run. The readout noise was measured to be 8.3 electrons/pixel for images taken at  $-40^\circ\text{C}$ , and changed to 8.2 as chip temperatures changed to  $-50^\circ\text{C}$ . But virtually no changes were found for temperatures lower than that. Therefore we concluded that readout noise is not sensitive to the chip temperature while bias level is.

Table 3 compares the measured values to those listed in the test report by the camera manufacturer. The values are similar to the ones quoted in the test report.

### 3.5. Shutter pattern

The mechanical shutter in front of our science camera takes a finite time to open and close when taking an image. This causes an imprint of the shutter pattern on the image when the exposure time is short.

To examine how the shutter pattern affects an exposure as a function of exposure time, we took a series of dome flats with different exposure times from 0.1 second to six seconds, which is shown in Fig. 16. The five winged shutter pattern is clearly seen in the 0.1 second exposure and it disappears as the exposures get longer. The shutter

pattern remains in the exposures up to four second long, and it does not appear in the longer exposure. The comparison of three second long exposure and eight second long exposure reveals that the central region of the three second image is about 0.4 % brighter than the edge due to the remaining shutter pattern. From this result, it is recommended to take flat images or science images with exposures longer than four seconds if a precise photometry better than 0.4 % is required. Or additional shutter pattern images should be taken as a part of calibration observation.

### 3.6. Linearity of the detector

As in other CCD imagers, our science camera shows non-linear behavior for the illumination near its full-well capacity. To find out the linearity range of CQUEAN detector, we obtained the images of the constant dome flat light at different exposure times. The experiment was repeated several times to check the stability of the non-linearity behavior.

The upper panel of Fig. 17 shows the readout values against different exposure times from the experiments carried out over two nights in March 2011. Since the dome flat light brightnesses were different from each other on two occasions, the resultant linearity curves show different slopes. However, they show similar patterns. In both experiments, CCD readout values are more or less linear up to  $\sim 50000$  ADUs. The linearity curves show non-linear behavior beyond this range. The pixel values show a little variable behavior on each occasion.

### 3.7. Example of a reduced CQUEAN image and the fringe pattern

The data reduction of CQUEAN can follow the standard procedures of bias and dark subtraction, followed by flat-fielding. For flat-fields, we recommend twilight flats, although dome flats can be used if the required photometric accuracy is not better than 0.02 mag. Also, one should be cautious about the temporal variation in the bias level. We recommend the users to take bias images just before and after the observation of each target and use these biases during the data reduction.

Fig. 18 shows an example of a raw and a reduced CQUEAN images in  $z$ -band. Fringe pat-

tern is caused by the interferences of the light reflected on the surface and inner silicon layer of the CCD chip, and is usually very severe in the image of red optical bands taken with backside-illuminated, thinned CCD (e.g., see Im et al. 2010a; Jeon et al. 2010). However, no fringe patterns were noticed in stacked CQUEAN images so far up to total integration time of two hours. We note that the standard reduction procedures removes most of the artifacts in the dark and flat-field, although the correction for the vignetted regions is not good.

## 4. ON-SKY PERFORMANCE

### 4.1. Optical performance

To estimate the optical performance of CQUEAN, we examined the stellar image profiles in five band images. For the test, we obtained the images of an open cluster, NGC 6644, during the 2010 August run. SExtractor was run on the raw images to obtain the image profile parameters such as FWHM, and ellipticity. Sources with stellarity  $\geq 0.95$  were regarded as point sources and their FWHM and ellipticity were examined against their distances from the image center. Fig. 19 displays the results for all sources including point sources. The optical performance of the focal reducer is optimized for the wavelength band between  $0.8 - 1.1 \mu m$ , therefore the sources on the  $g$  and  $r$ -band images have much larger FWHMs than on the other band images and show coma aberration: their FWHMs get larger and their image profiles become more elongated as they are further from the image center. The coma is corrected for longer wavelength bands and it cannot be seen for the  $z$  and  $Y$ -band images. This result indicates that while most region of the chip can be used for photometry of faint sources for wavelength bands longer than  $i$ -band, one should be cautious about using the outer part of the  $g$  or  $r$ -band images (radius  $\geq 200$  pixels). On short exposure frames under excellent seeing, we recorded  $0.6''$  FWHM for point sources, demonstrating the good optical performance of the focal reducer.

### 4.2. CQUEAN sensitivity

We estimated the sensitivity of the CQUEAN science camera, from the data of BD+47 0478 (Fukugita et al. 1996), one of fundamental stan-



dard stars for SDSS, obtained during the 2010 August run. The sensitivity of the system depends on the throughput of the optical components and the QE of the detector. Table 4 lists the limiting magnitude during the bright time (full moon illumination) and the dark time, for one hour total integration with  $5\text{-}\sigma$  error.

The listed sky count rate is helpful when one wants to observe their targets in the sky-limited regime. Since the dark current is only 0.3 ADU/sec/pixel, the dominant source of the noise is either the sky background noise or the read-out noise in case of faint targets. Considering the readout noise of 8.2 ADU and sky brightness in Table 4, observations with exposure time longer than 5 – 15 seconds are limited by the sky background noise.

The expected overall throughput of CQUEAN can be calculated with data listed in Table 5, and compared with actual measurement values in Fig. 20. The expected value takes into account of the reflectivity of the two telescope mirrors, transmittance of the four lenses in focal reducer and the camera window, and the QE of the CCD chip. Note that we could not include the wavelength dependent throughputs of the AR coating on the surfaces of the focal reducer lenses which had not been provided by the manufacturer. The actual overall throughput turned out to be 80 – 85 % of what is expected in  $i$ -band to  $z$ -band. The throughput is especially lower at shorter wavelength bands: 25 % at  $g$ , and 40 % at  $r$ -band. The reduced performance in these two bands is caused by the AR coating of focal reducer lenses optimized for longer wavelength bands.

### 4.3. Cosmic ray hits

Deep depletion CCD is known to be more susceptible to cosmic ray hits than the back illuminated thinned CCDs. Therefore we tried to estimate how much the cosmic ray hits can affect our science mission with CQUEAN. To get a general idea of how severe the cosmic ray hits might be on a single image, we identified cosmic ray hits with `L.A.Cosmic` (van Dokkum 2001), a cosmic ray removal program for a single frame image, on 73 frames of 300 second exposure taken with  $g$ ,  $z$ , or  $Y$ -filter during a CQUEAN run. We found that similar number of pixels are hit by the cosmic rays among all filter images:  $83.1 \pm 37.1$  for

$g$ ,  $118.6 \pm 42.5$  for  $z$ , and  $110.6 \pm 40.9$  pixels for  $Y$ -band images. These values correspond to about 0.01 % of total area. The affected pixels are easily removed during the stacking of multiple frames or with other cosmic ray removal programs. Therefore we concluded that cosmic ray hits do not affect our scientific mission of CQUEAN.

## 5. SCIENTIFIC CAPABILITY OF CQUEAN

Since 2010 August, CQUEAN has been used to obtain photometric data for many scientific applications. Scientific targets include quasar candidates at  $z = 5.0 - 5.7$ , transients such as Gamma Ray Bursts (GRB), supernovae, and variable young stellar objects, and host galaxies of bright quasars. Here, we summarize some of these observations briefly, in order to demonstrate the CQUEAN scientific capabilities.

### 5.1. Stephan’s Quintet

Multi-band images of the Stephan’s Quintet was obtained as a part of the science verification in our first run. Fig. 21 shows  $r - i - z$  color composite image of Stephan’s Quintet. The image shows the expected optical performance of CQUEAN.

### 5.2. Transient observation

CQUEAN has been used to observe afterglows of GRBs (Im et al. 2011, 2010b,c; Jeon et al. 2011; Park et al. 2010) as a part of our GRB afterglow observation project (e.g., Lee et al. 2010). Most of the GRBs were observed with  $r$ ,  $i$ , and  $z$ -band, and in some cases with  $Y$ -band. Upon the observation, preliminary photometry was reported to the GCN circular, and for some targets, the final photometric results were contributed to collaborative GRB studies. We are also carrying out a long-term monitoring of Swift J1644+57 (Burrows et al. 2011) in multi-wavelength bands with many instruments including CQUEAN (Im et al. 2011), to understand the evolution of stellar remnants near a supermassive blackhole. Fig. 22 shows an  $i$ -band image of GRB 100816A taken about eight hours after its detection by Swift (Gehrels et al. 2004). The total integration time of the image is 2400 seconds. From this image, we were able to separate the GRB afterglow and its host galaxy which is about  $i = 20.58$  AB magnitude and located only  $1.3''$

from the afterglow (Im et al. 2010b). Another image of a GRB afterglow is shown in Fig. 23, where we present  $r$ ,  $i$ , and  $z$ -band images of GRB 101225A (Park et al. 2010). The CQUEAN data were used to characterize the early evolution of the optical afterglow which turn out to be dominated by a black-body radiation (Thöne et al. 2011).

### 5.3. High redshift quasar candidates

We have been performing a survey of quasars at  $5.0 < z < 5.7$  using two custom designed filters. About 1000 targets were observed with the custom  $is$  and  $iz$ -bands, among which about 20 were identified as promising candidates based on their colors from CQUEAN and mid infrared (MIR) colors of Wide-field Infrared Survey Explorer (WISE) (Wright et al. 2010) data. Fig. 24 shows the locations of those candidates on the color-color diagram along with other targets observed.

## 6. SUMMARY

We developed CQUEAN, an optical CCD camera system which has an enhanced sensitivity at  $\sim 1 \mu m$  compared to the conventional CCD camera. CQUEAN consists of a science camera, seven filters, a focal reducer to enlarge its field of view, and a guide camera system. CQUEAN also includes its in-house GUI software for controlling the instrument. It is attached at the Cassegrain focus of the 2.1 m telescope at McDonald Observatory, USA.

The analysis of the CQUEAN data reveals that the camera is stable and it meets the requirements set by the scientific purpose. With the focal reducer of our own design, the camera produces images of the seeing as good as  $0.6''$  without any fringe pattern in longer wavelength bands, although coma aberration is present for  $g$  and  $r$ -band images as expected. We estimated the sensitivity of the camera to be  $z = 23.4$  AB mag. at one hour integration. In addition, the characteristics of bias, dark, and flat images of the science camera are examined, and the observation and data reduction strategy is discussed to obtain better results under these system characteristics. We also find that CQUEAN can obtain images of exposures up to 1200 second with its auto-guider system.

With the enhanced sensitivity at NIR together with a field of view of  $4.8' \times 4.8'$ , CQUEAN has

been serving as a useful instrument for the observation of red, astronomical objects such as high redshift quasar candidates, afterglows of GRBs, and supernovae.

This work is supported by the Creative Research Initiatives program of the Korea Science and Engineering Foundation (KOSEF), grant No. 2009-0063616, funded by the Korea government (MEST). This paper made use of the data obtained with a telescope at the McDonald Observatory, TX, USA. We thank the staffs of McDonald Observatory, including David Doss and John Kuehne, for their assistance of CQUEAN observations, and P. Samuel Odoms for allowing us to use *agdr*, the auto-guiding software. Authors also thank observers who helped obtain the data discussed in the paper.

## REFERENCES

- Bertin, E., & Arnouts, S. 1996, *A&AS*, 117, 393
- Birney, D. S., Gonzalez, G., & Oesper, D. 2006, *Observational Astronomy* (2nd ed.; Cambridge: Cambridge University Press)
- Burrows, D. N., et al. 2011, *Nature*, 476, 421
- Doss, D. 2011, private communication
- Fukugita, M., Ichikawa, T., Gunn, J. E., Doi, M., Shimasaku, K., & Schneider, D. P. 1996, *AJ*, 111, 1748
- Gehrels, N., et al. 2004, *ApJ*, 611, 1005
- Hillenbrand, L. A., Foster, J. B., Persson, S. E., & Matthews, K. 2002, *PASP*, 114, 708
- Im, M., Park, W.-K., Pak, S., Baek, G., & Oh, Y. 2011, *GCN Circ.*, 12295, 1
- Im, M., Ko, J., Cho, Y., Choi, C., Jeon, Y., Lee, I., & Ibrahimov, M. 2010a, *JKAS*, 43, 75
- Im, M., et al. 2010b, *GCN Circ.*, 11108, 1
- Im, M., et al. 2010c, *GCN Circ.*, 11153, 1
- Jeon, Y., Im, M., Pak, S., & Jeong, H. 2011, *GCN Circ.*, 11967, 1
- Jeon, Y., Im, M., Ibrahimov, M., Lee, H. M., Lee, I., & Lee, M. G. 2010, *ApJS*, 190, 166

Kim, E., et al. 2011, JKAS, 44, 115  
Lee, I., Im, M., & Urata, Y. 2010, JKAS, 43, 95  
Lim, J., et al. 2012, in preparation  
Lawrence, A., et al. 2007, MNRAS, 379, 1599  
Mortlock, D. J., et al. 2011, Nature, 474, 616  
Park, W.-K., Im, M., Choi, C., Jeong, H., Lim, J.,  
& Pak, S. 2010, GCN Circ., 11594, 1  
Thöne, C. C., et al. 2011, Nature, 480, 72  
van Dokkum, P. G. 2001, PASP, 113, 1420  
Wells, D. C., Greisen, E. W., & Harten, R. H.  
1981, A&AS, 44, 363  
Wright, E. L., et al. 2010, AJ, 140, 1868  
York, D. G., et al. 2000, AJ, 120, 1579

TABLE 1  
SPECIFICATION OF ANDOR iKON-M M934 BR-DD CAMERA<sup>†</sup>

Type of CCD chip	A deep-depletion chip made by E2V
Pixel number	1024 × 1024
Pixel size	13 μm × 13 μm
Image area	13.3 mm × 13.3 mm
Pixel scale <sup>a</sup>	0.281"/pixel
Field of view <sup>a</sup>	4.8' × 4.8'
Active area pixel well depth	100,000 e- (typical)
Output saturation	200,000 e- (typical)
Pixel readout rate	2.5, 1.0 <sup>b</sup> , 0.05 MHz
Array readout time	~ 0.5, 1, 20 seconds
Pixel readout noise (typical)	9.0, 7.0, 2.8 electrons
Digitization	16 bit at all readout speeds
Cooling	Down to -80 °C with air-cooling Down to -100 °C with optional water-cooling

<sup>†</sup>Based on the brochure

<sup>a</sup>With focal reducer

<sup>b</sup>Current readout speed for CQUEAN

TABLE 2  
DESCRIPTIONS OF THE FOCAL REDUCER.

Surface <sup>a</sup>	Description	Medium	Radius of curvature <sup>b</sup>	Thickness <sup>b</sup>	Diameter <sup>b</sup>
1	Lens 1	N-BAF10 <sup>c</sup>	91.188	14.00	66.00
2	Lens 2	N-SF66 <sup>c</sup>	-118.153	4.00	66.00
3	...	...	118.153	8.20	63.00
4	Lens 3	SF57 <sup>c</sup>	84.927	11.00	66.00
5	...	...	Infinity	15.80	66.00
6	Lens 4	N-FK5 <sup>c</sup>	43.774	7.00	50.00
7	...	...	31.344	43.03	42.00
8	Filter	Silica	Infinity	5.00	28.00
9	...	...	Infinity	23.58	28.00
10	CCD	...	Infinity	...	...

<sup>a</sup>See Fig. 3 for the surface numbers.

<sup>b</sup>All values are in unit of millimeter.

<sup>c</sup>Optical glasses manufactured by Schott.

TABLE 3  
CHARACTERISTICS OF THE CCD IN THE SCIENCE CAMERA

	Measured	Reported <sup>†</sup>
Gain (e-/ADU)	$1.0 \pm 0.1$	1.2
Readout noise (e-/pixel)	$8.2 \pm 0.1$	7.0
Dark level (e-/sec/pixel)	$0.23 \pm 0.01$	0.1
Saturation level (e-/pixel)	$\sim 57000$	75957
Base level (ADU)	4425 $\sim$ 4487	4632

<sup>†</sup>Tested and reported by the camera manufacturer. The camera was cooled down to  $-80^\circ\text{C}$  for the measurement.

TABLE 4  
CQUEAN POINT-SOURCE SENSITIVITY<sup>a</sup>

Condition	Filter	$\lambda_{eff}$ ( $\mu\text{m}$ )	Sky count (DN/sec/pixel)	Sky brightness (mag/arcsec <sup>2</sup> )	Magnitude limit <sup>b</sup> (AB mag)
Dark time	<i>r</i>	0.623	1.2	21.3	24.1
	<i>i</i>	0.768	4.6	20.6	24.3
	<i>is</i>	0.739	5.0	20.3	24.0
	<i>iz</i>	0.849	8.0	19.8	23.8
	<i>z</i>	0.877	5.2	19.6	23.4
	<i>Y</i>	0.991	3.8	18.5	22.1
Bright time	<i>r</i>	0.623	4.1	19.8	23.4
	<i>i</i>	0.768	11.1	19.7	23.8
	<i>is</i>	0.739	8.4	19.7	23.7
	<i>iz</i>	0.849	11.7	19.3	23.5
	<i>z</i>	0.877	8.4	19.1	23.1
	<i>Y</i>	0.991	6.2	17.9	21.8

<sup>a</sup>Based on the data obtained on 2010 August run

<sup>b</sup>With total one hour integration and  $5\text{-}\sigma$  error

TABLE 5  
THE THROUGHPUT ESTIMATION FOR CQUEAN

Filter	Expected				Measured
	Telescope <sup>a</sup>	Focal reducer <sup>b</sup>	Camera <sup>c</sup>	Combined	
<i>g</i>	0.840	0.934	0.52	0.40	0.10
<i>r</i>	0.820	0.984	0.72	0.58	0.23
<i>is</i>	0.780	0.991	0.82	0.63	0.44
<i>i</i>	0.762	0.991	0.82	0.62	0.49
<i>iz</i>	0.783	0.991	0.72	0.53	0.46
<i>z</i>	0.766	0.991	0.64	0.49	0.42
<i>Y</i>	0.861	0.993	0.22	0.19	0.12

<sup>a</sup>Effective throughput of two mirrors, based on the reflectivity measured on 2011 May (Doss 2011)

<sup>b</sup>Effective throughput of four lenses, based on the generic transmittance for the lens material used in the focal reducer. Note that the throughput of the AR coatings on the focal reducer lenses are not included.

<sup>c</sup>Effective throughput of camera window and CCD QE, based on the generic data.

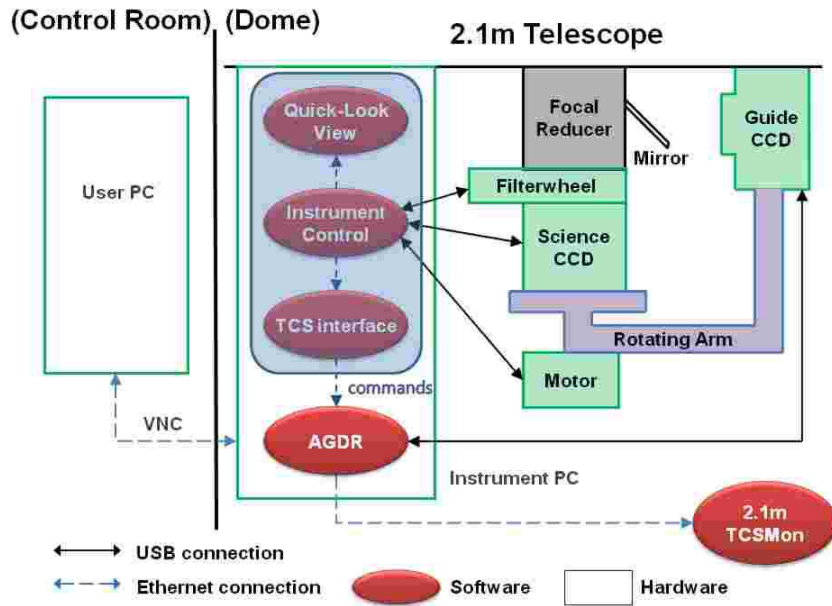


Fig. 1.— System architecture of the CQUEAN system (Kim et al. 2011). The ellipses and the squares denote the software and the hardware parts, respectively. The arrows indicate the directions of command and data flows. All units of CQUEAN including the control computer are attached to the telescope Cassegrain focus. The observers access the control computer from the control room via an ethernet network.

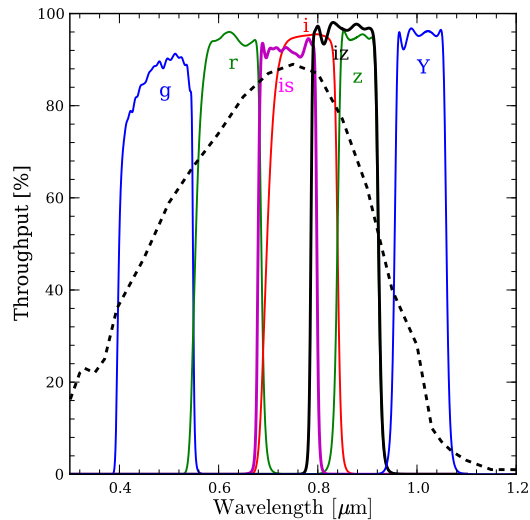


Fig. 2.— QE of the science camera chip and the throughputs of the CQUEAN filters. CCD QE is shown with black dashed line, while throughputs of filters are shown with solid lines.

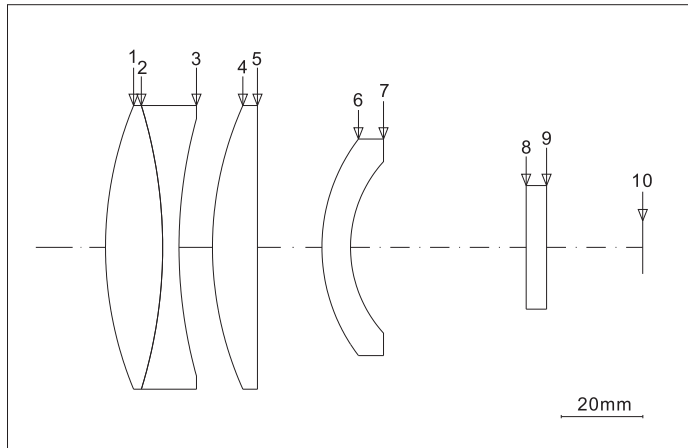


Fig. 3.— Optical layout of the focal reducer. See Table 2 for the descriptions of the optical elements.

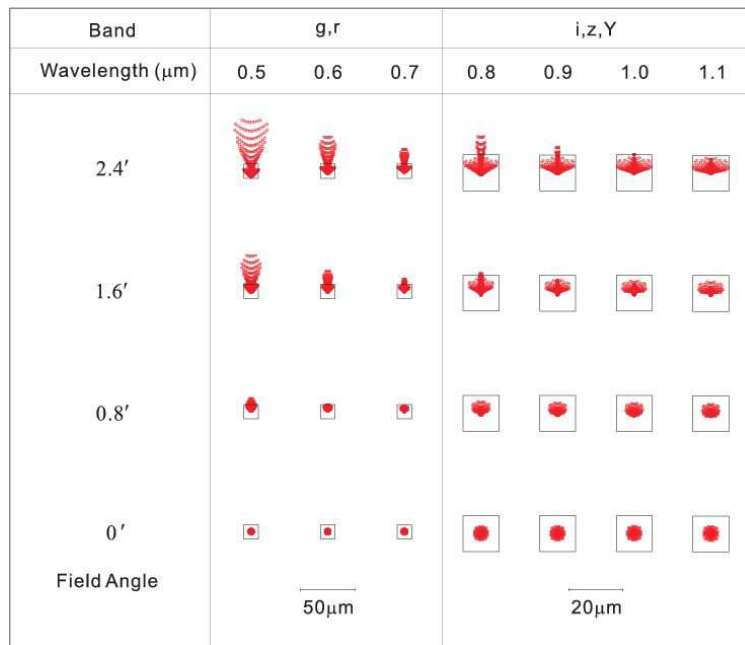


Fig. 4.— Spot diagrams for each wavelength band at its focal plane position. The sizes of the square boxes are the same with that of a single CCD pixel.



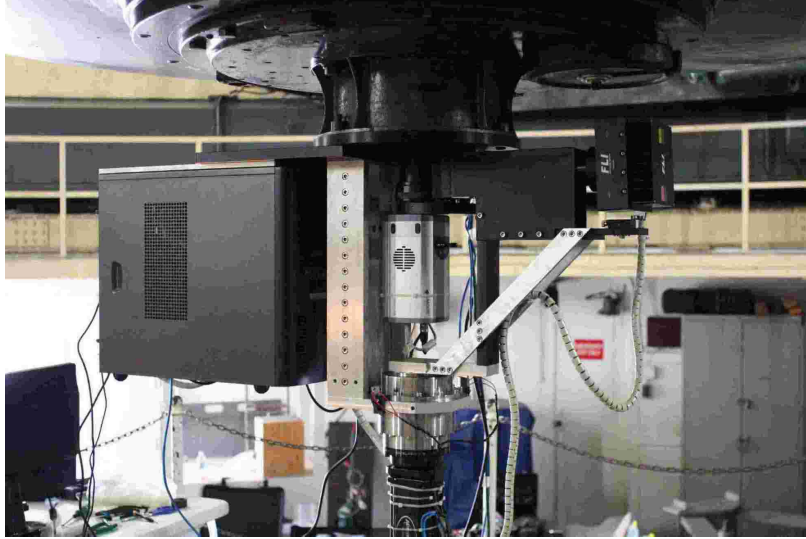


Fig. 5.— CQUEAN system attached to the Cassegrain focus of 2.1 m telescope. The black box on the left is the control computer, and a small silver box at the center is the science camera. Motor below the science camera controls the guide camera arm that holds the guide camera, a small black box on the right part of the photo.

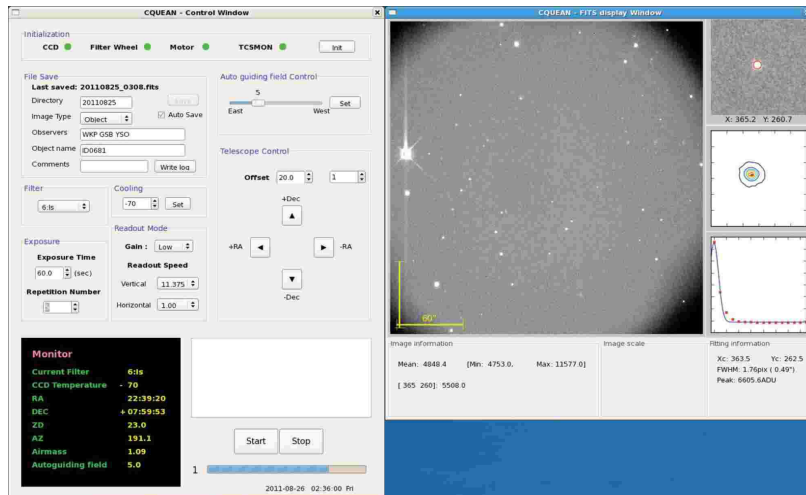


Fig. 6.— Screenshot of CQUEAN control program running on a linux machine. The left window is the CQUEAN Control window, and the right one Quick-Look window.

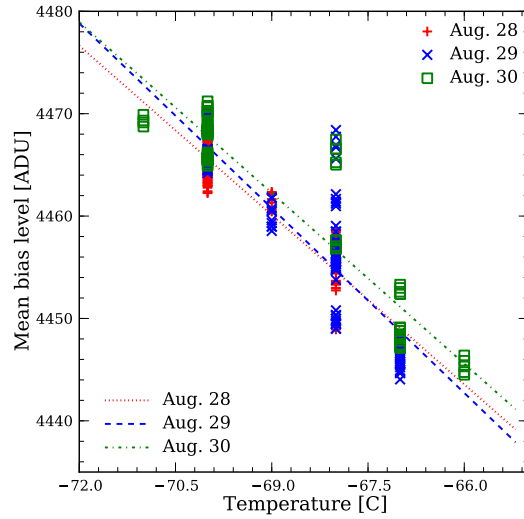


Fig. 7.— Bias level of CQUEAN during three nights of 2011 August run against the chip temperature. The each point in this plot represents the mean pixel value of a single bias image. Bias images were obtained usually before and after the observation of a target. The three lines indicate the fitted relation to samples from each night.

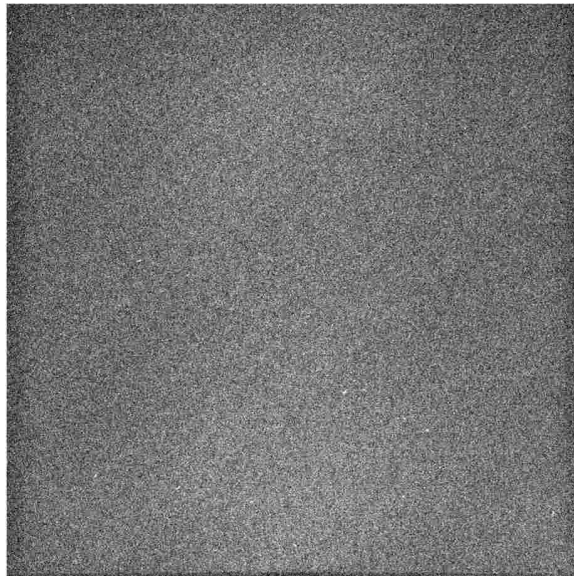


Fig. 8.— Example of bias subtracted 300 second dark images of CQUEAN.

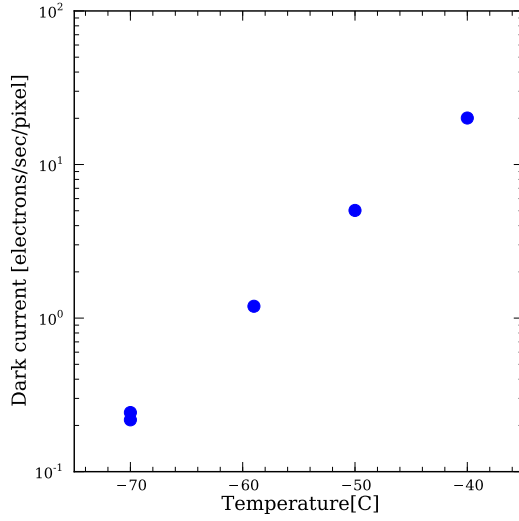


Fig. 9.— Dark current levels of science camera against the cooling temperature. The plot indicates that the dark current increases by a factor of ten when the temperature increases by  $10^\circ\text{C}$ .

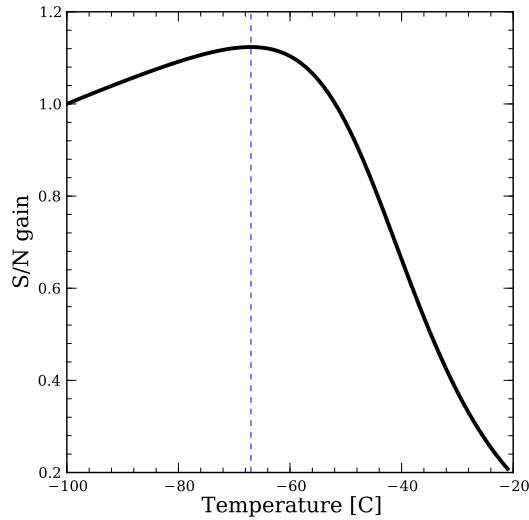


Fig. 10.— Signal to noise ratio improvement relative to that in  $-100^\circ\text{C}$  with respect to CCD cooling temperature for a 300 second observation of a faint source in  $1\ \mu\text{m}$  band. The vertical dashed line indicates the temperature with the maximum signal to noise ratio improvement. The QE of the chip is assumed to be linear to the temperature. The dark level shown in Fig. 9, and the a sky background value shown in Table 4 was used in the calculation.

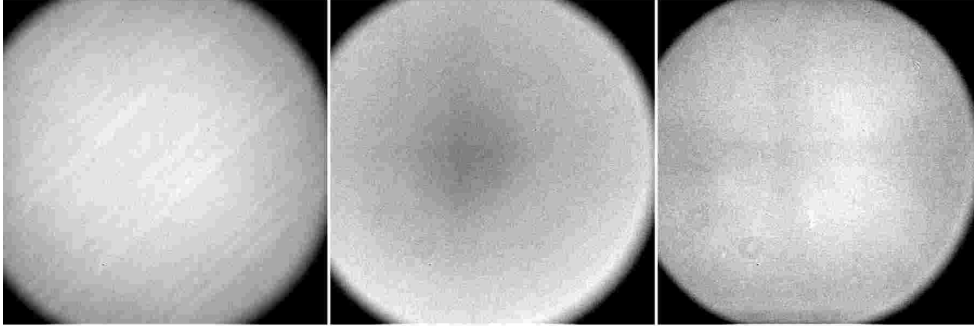


Fig. 11.— Examples of flat images for  $g$ -band (right),  $r$ -band (middle), and  $Y$ -band (left). All flat images show vignetting due to the focal reducer and the filters at all four corners. For  $g$  and  $r$ -bands, flat images show a inclined line patterns. Flat images in other band look very similar to  $Y$ -band flat image.

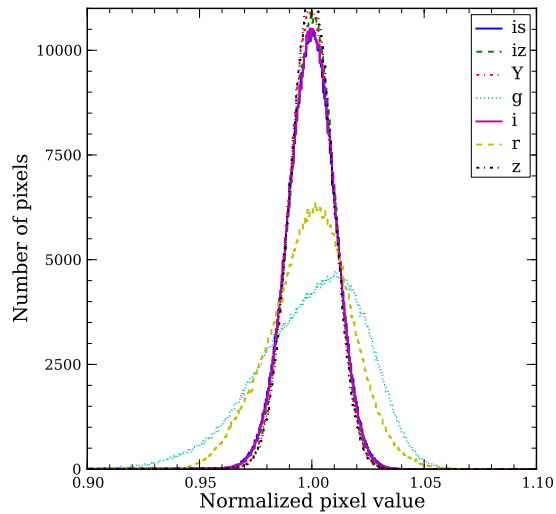


Fig. 12.— Distributions of normalized pixel values in the flat images for each filter. Note vignettted regions are not included in the distribution.

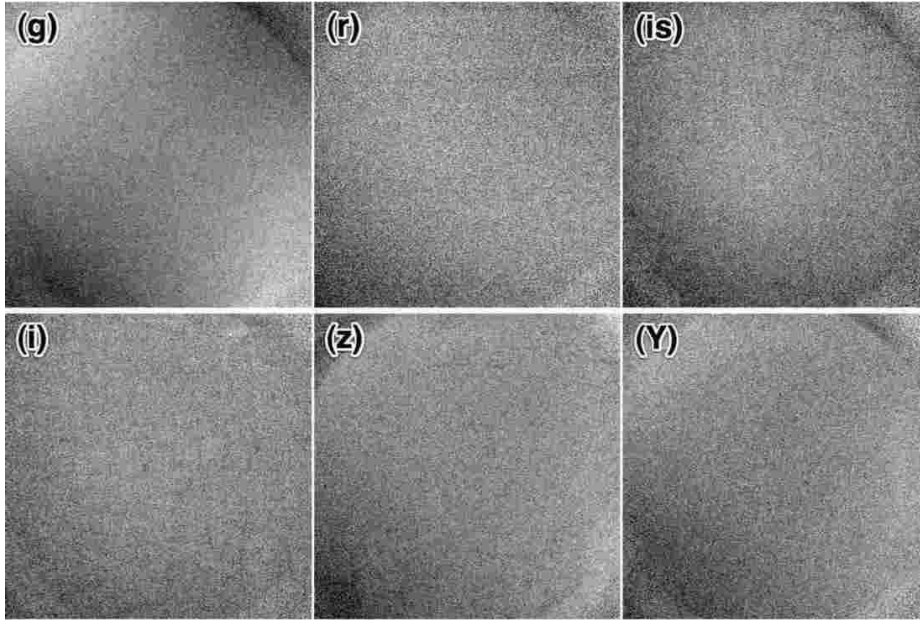


Fig. 13.— Images of twilight flats taken on 2011 Aug. 28 divided by the ones taken on 2011 Aug. 30. In all the images vignetting pattern is seen clearly at image corners. Gradient from lower left to upper right direction is seen in this particular example sets but patterns vary on different nights. See Section 3.3 for detailed explanation.

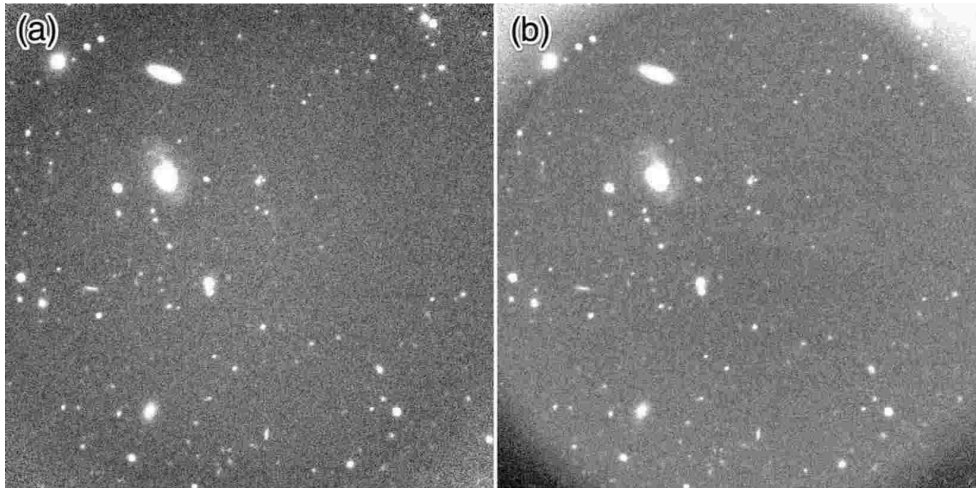


Fig. 14.— *i*-band image (1800 seconds, total integration) flattened (a) with twilight flat, and (b) with dome flat. All the images including the flats were taken at the same night. See Section 3.3 for the detailed explanation on the difference of dome flat and sky flat.

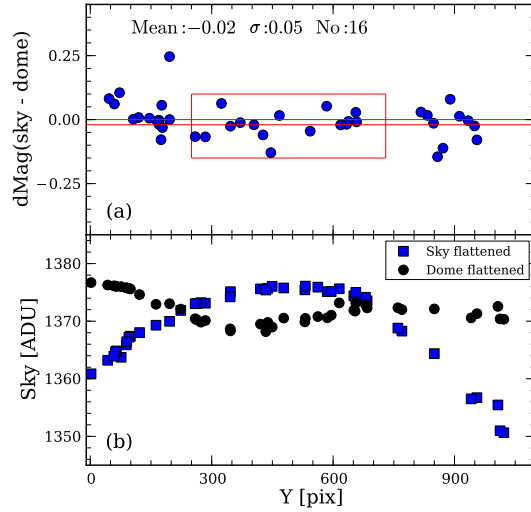


Fig. 15.— (a) Magnitude difference between the photometry of the samples which S/N is greater than 10 on both images shown in Fig. 14, along the Y axis of the image chip. The red box indicates the samples used in derivation of mean value written in the upper part of the panel. The samples near the both ends of Y axis are not used since all of them are located in vignetted region. (b) Sky background around the sources detected in the central columns ( $X = 400 - 600$ ), along the Y axis of the image.

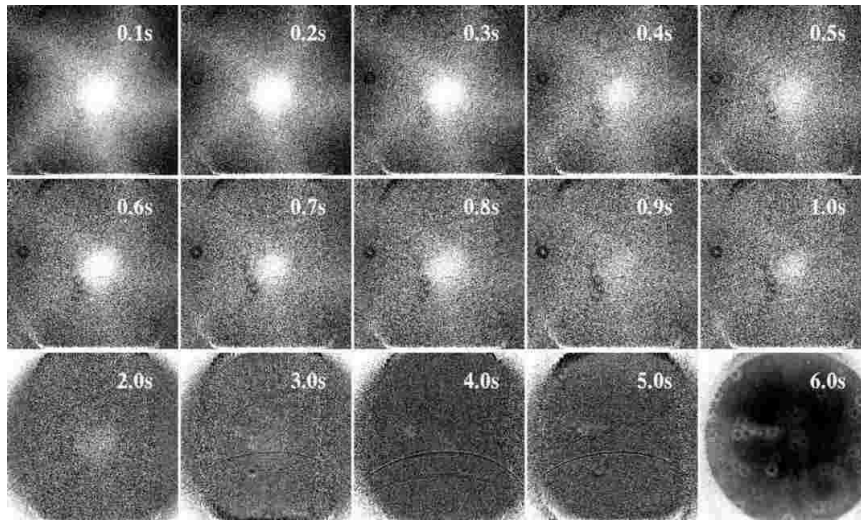


Fig. 16.— Dome flat images of various exposures showing the shutter patterns. Shutter pattern survives up to 3.0 second image.

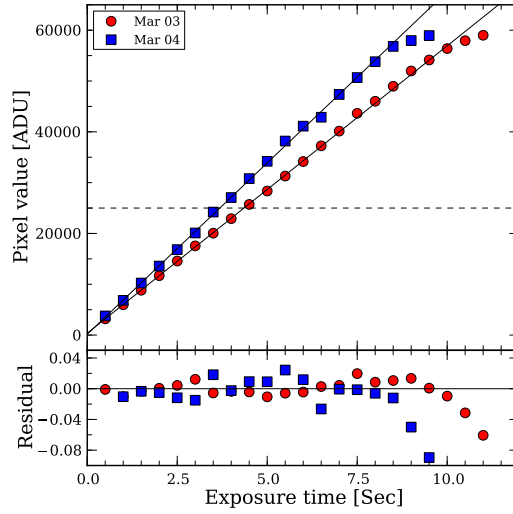


Fig. 17.— Upper panel shows the CCD readout values against the exposure times of constant dome flat light. The dashed horizontal line indicates the upper limit of the readout values used to fit the linear relations shown as solid lines in the figure. The lower panel shows the residuals between the measured value and fitted line with respect to measured value, against the exposure times.

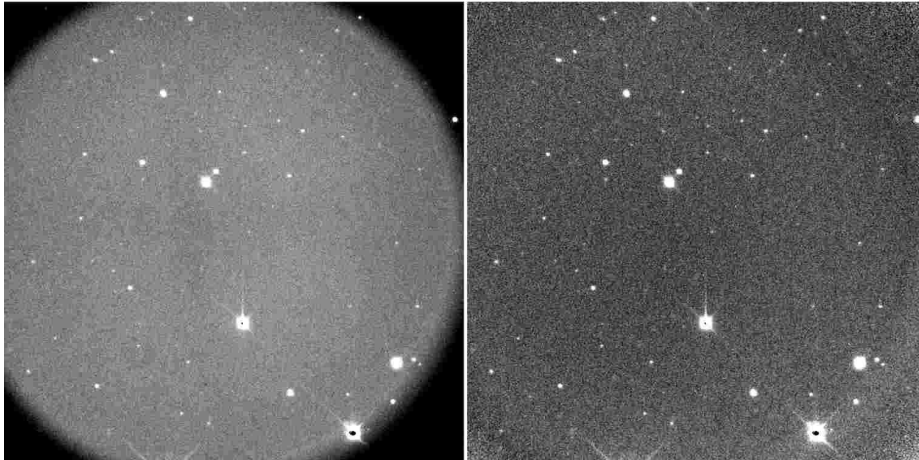


Fig. 18.— Examples of a  $z$ -band raw CQUEAN image (left) and a reduced one (right). Note that fringe pattern is not seen on both images. Although most of the system footprints are removed in the reduced image, hint of vignetting is still seen at its corners.

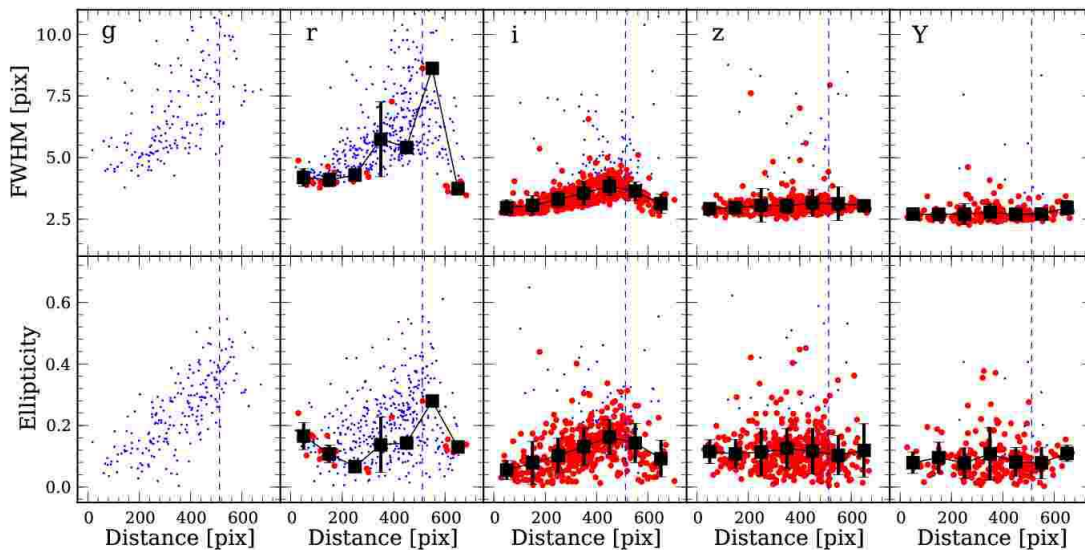


Fig. 19.— FWHM (upper panels) and ellipticity (lower panels) of detected sources in NGC 6633 images taken with CQUEAN. Vertical dashed line in each panel indicates the range where vignetting is not present. The blue dots represent all sources detected in the images, and red filled circles denote the ones classified as point sources by SExtractor. Black squares represent the mean values for the sources at every 100 pixel interval from the CCD array center.  $1\text{-}\sigma$  ranges are indicated with vertical error bars.

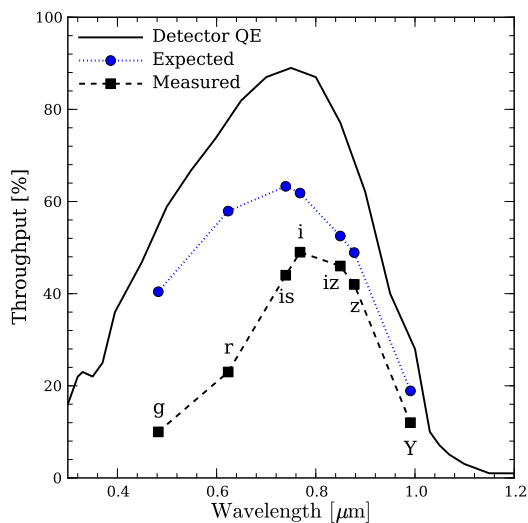


Fig. 20.— Measured overall throughput of CQUEAN system. The solid line represents the QE of the science camera chip alone, and the dotted line with circular points the expected throughput from the combination of those for the chip QE, camera window, filters and two mirrors in the telescope. The dashed line with square points represents the measured overall throughput.





Fig. 21.— Composite color image of Arp 319 made from  $r$ ,  $i$ , and  $z$ -band images taken with CQUEAN. Some rows in upper part of image were trimmed in the final product. A faint arc line remains in the lower part of the image after the reduction, which is due to inappropriate vertical shift speed setting of the camera.

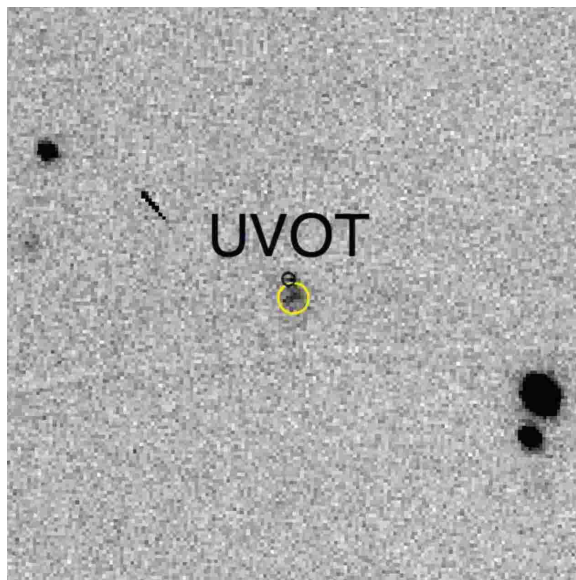


Fig. 22.— Portion of  $i$ -band image of GRB 100816A and its host galaxy taken by CQUEAN. Black circle shows the position of GRB 100816A afterglow detected by UVOT onboard Swift, with which radius denotes its uncertainty. The extended emission (marked with yellow circle) just below the UVOT position comes from the host galaxy of GRB 100816A.

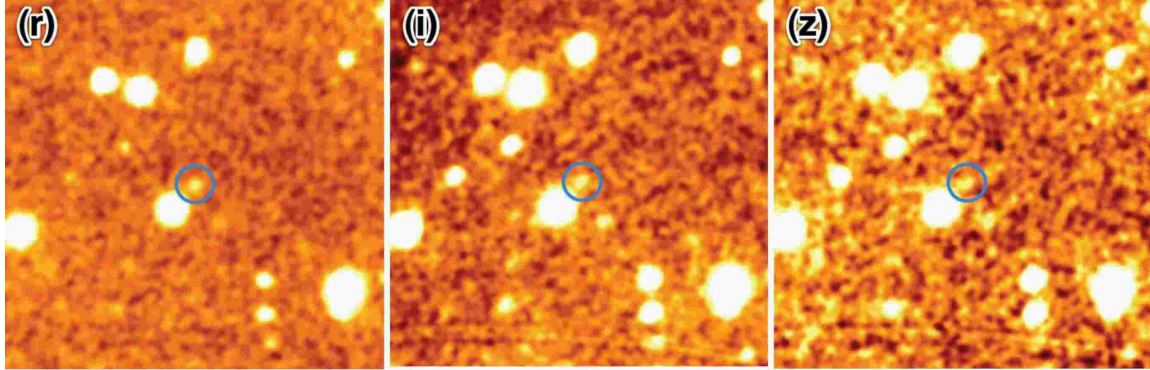


Fig. 23.— Images of GRB 101225A taken by CQUEAN with  $r$  (left),  $i$  (middle), and  $z$  (right) filters. The field of view of each image is about  $1.1' \times 1.1'$ , and the target is located within the blue ring in the center. All images were smoothed to enhance the contrast.

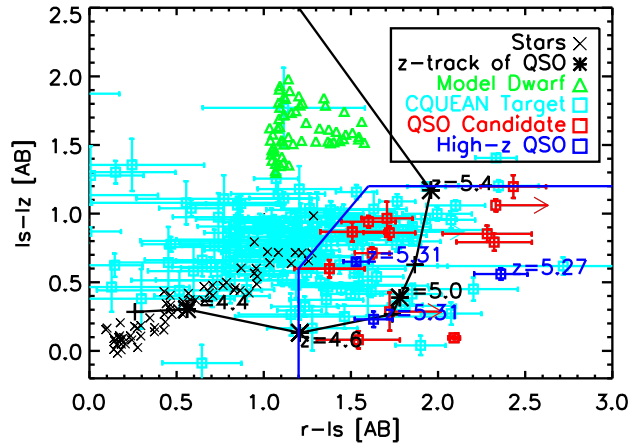


Fig. 24.— Color-color diagram of the various targets.  $is$  and  $iz$  magnitudes were obtained with CQUEAN, while  $r$  magnitude was obtained from SDSS catalog. The black line shows the track of quasars as a function of their redshifts. The lower right region designated with blue lines indicates the color selection criteria for initial quasar candidate samples. Note that previously known quasars, shown as blue open squares, all fall on the selection region. The final quasar candidates, shown with red open squares, were selected from this color criteria in combination with MIR colors.